Control of conductivity in Fe-rich cobalt-ferrite thin films with perpendicular magnetic anisotropy

Masaya Morishita,[1] Tomoyuki Ichikawa,[1] Masaaki A. Tanaka ◉,[1,*] Motoharu Furuta,[1]
Daisuke Mashimo,[1] Syuta Honda ◉,[2,3] Jun Okabayashi ◉,[4] and Ko Mibu ◉[1]

[1]*Graduate School of Engineering, Nagoya Institute of Technology, Nagoya, Aichi 466-8555, Japan*
[2]*Department of Pure and Applied Physics, Kansai University, Suita, Osaka 564-8680, Japan*
[3]*Center for Spintronics Research Network, Graduate School of Engineering Science, Osaka University, Toyonaka, Osaka 560-8531, Japan*
[4]*Research Center for Spectrochemistry, The University of Tokyo, Bunkyo-ku, Tokyo 113-0033, Japan*

We fabricated two types of cobalt-ferrite (001) thin films, insulative Fe-rich cobalt-ferrite $Co_xFe_{3-x}O_{4+\delta}$ (I-CFO) and conductive Fe-rich cobalt-ferrite $Co_yFe_{3-y}O_4$ (C-CFO), with perpendicular magnetic anisotropy (PMA) on MgO (001) substrates. Although the stoichiometric cobalt ferrite is known as an insulating material, it is found that the conductivity of Fe-rich cobalt ferrites can be controlled by changing the source materials and deposition conditions in the pulsed laser deposition technique. The I-CFO and C-CFO films exhibit PMA through the in-plane lattice distortion. We investigated the Fe-ion-specific valence states in both I-CFO and C-CFO films by Mössbauer spectroscopy and x-ray magnetic circular dichroism and found that the difference in conductivity corresponds to the abundance ratio of the Fe^{2+} state at the octahedral *B*-site (O_h) in the inverse spinel structure. Furthermore, first-principles calculations reproduce the changes in the density of states at the Fermi level depending on the cation vacancies at the *B*-site, which explains the difference in conductivity between I-CFO and C-CFO.

I. INTRODUCTION

Spinel-type cobalt ferrites [$CoFe_2O_4$ (CFO)] have been investigated for a long time for magnetic applications as magnetic insulators with high-frequency performance, magnetostrictive properties, and so on, in the forms of bulk, powder, and thin films, because of their insulating advantages [1–13]. They have an inverse spinel structure in AB_2O_4 chemical formulation, with Fe^{3+} at the tetragonal *A*-site (T_d) and Fe^{3+} and Co^{2+} at the octahedral *B*-site (O_h). Recent developments in spintronics boost the application of thin CFO films stacked with other nonmagnetic and magnetic layers, which are, for example, utilized as spin-filtering tunnel barriers [14–19]. There are some reports that CFO (001) films exhibit perpendicular magnetic anisotropy (PMA) under tensile epitaxial strain [20–35]. Materials with PMA are strongly demanded for high-density recording techniques. Therefore, CFO films can be some of the best candidates for the PMA system without rare-earth elements. The PMA in CFO films is thought to originate from Co^{2+} ($3d^7$) at the octahedral *B*-site (O_h) in the tetragonally distorted inverse spinel structure [30]. Furthermore, it is reported that the squareness of the hysteresis curves, i.e., the abruptness in magnetization reversal, is improved in Fe-rich CFO films [28]. The valence states of the cations in these stoichiometric and Fe-rich CFO films can be examined by site-specific analyses such as x-ray magnetic circular dichroism (XMCD) [25,35] and Mössbauer spectroscopy (MS) [7,33]. For the charge neutrality, the formal valence states are recognized as Co^{2+} (O_h),

Fe^{3+} (O_h), and Fe^{3+} (T_d) in stoichiometric CFO films [9]. However, the substitution of Co^{2+} by Fe^{2+} promotes the formation of Fe^{2+} (O_h) sites, which induces the conductive properties in CFO films. The conductivity in CFO films would arise depending on the compositions due to the formation of Fe^{2+} states through $Co^{2+} \rightarrow Fe^{2+}$ substitution, which is regarded as an approach to magnetite Fe_3O_4. On the other hand, insulative CFO can be grown by $Co^{2+} \rightarrow Fe^{3+}_{2/3} \square_{1/3}(\square =$ cation vacancies) substitution, which is an approach to insulative maghemite γ-Fe_2O_3 [4,33,36]. Hereafter, we refer to insulative Fe-rich cobalt-ferrite $Co_xFe_{3-x}O_{4+\delta}$ as I-CFO and conductive Fe-rich cobalt-ferrite $Co_yFe_{3-y}O_4$ as C-CFO. The cation vacancies in I-CFO are expressed as excess oxygen with the symbol of δ.

The I-CFO films with PMA can be used as spin-filtering tunnel barriers to create perpendicularly spin-polarized electronic currents [19]. For this purpose, epitaxial I-CFO (001) films with in-plane tensile strain have to be grown on conductive underlayers. To develop fully epitaxial spin-filtering magnetic tunnel junctions (MTJs), the interfacial matching between conductive underlayers and I-CFO insulating barriers must be examined carefully. From the viewpoints of the lattice match and PMA stabilization, C-CFO layers with PMA are highly promising as conductive electrode layers under I-CFO barriers. Although the use of Fe_3O_4, which is conductive through the electron hopping between Fe^{2+} and Fe^{3+} ions, as electrode layers of conventional MTJs with nonmagnetic barriers has been reported recently [37,38], PMA properties can also be appended to oxide spintronics research by using Fe-rich I-CFO and C-CFO films. In fact, the MTJ combining both I-CFO tunnel barriers and C-CFO electrode layers achieved a large tunnel magnetoresistance (TMR) ratio of

*Corresponding author: mtanaka@nitech.ac.jp

-20% at 100 K [19]. To develop I-CFO and C-CFO films with PMA for high-quality Co-ferrite MTJs, the exact selective growth conditions for both I-CFO and C-CFO films and their detailed electronic states must be examined precisely.

Despite the realization of large PMA in CFO films on MgO substrates, it is known that the magnetic properties of epitaxial films of spinel ferrites are strongly affected by the existence of an antiphase boundary (APB). Until now, the APB in Fe_3O_4 films grown on MgO substrates fabricated by various methods was examined [39–43]; the APB broadens the abruptness in magnetization curves (MH curves) with the suppression of saturation magnetization M_s values. The APB in CFO films on MgO substrates is also discussed [4,25]. Although PMA was indicated by the magnetic hysteresis (MH) curves in these experiments, the magnitude of M_s is much smaller than that of bulk $CoFe_2O_4$. Therefore, the existence of APB in the spinel-type lattice structure is inevitable, and it would affect the MH curves. These facts must be considered also for the I-CFO and C-CFO cases.

In this paper, we aim to establish the selective film growth methods between insulative and conductive Fe-rich cobalt-ferrite films with PMA and discuss the origin of conductive properties from the results of transport measurements and site-specific magnetic spectroscopies of XMCD and MS.

II. EXPERIMENTAL

Single-crystalline I-CFO $(Co_xFe_{3-x}O_{4+\delta})$ and C-CFO $(Co_yFe_{3-y}O_4)$ films of 20 nm in thickness with various Co compositions ($x = 0.00, 0.11, 0.23, 0.36, 0.43, 0.56, 0.66, 0.76, 0.87$, and 1.00; and $y = 0.00, 0.23, 0.42$, and 0.66) were grown on MgO (001) substrates by a pulsed laser deposition (PLD) method using source materials with different powder compositions. The source materials for I-CFO, except $x = 0$, were prepared by mixing $CoFe_2O_4$ and Fe_3O_4 powder, and those for C-CFO, except $y = 0$, were by mixing $CoFe_2O_4$ and α-Fe powder. Pure Fe_3O_4 powder was used for the source materials of I-CFO with $x = 0$ and C-CFO with $y = 0$. The compositions between the Co and Fe atoms were controlled by the ratios of the source materials and confirmed by an electron probe microanalyzer. After the pressing process under 20 MPa, the I-CFO and C-CFO sources were baked in an atmospheric environment for 12 h at maximum temperatures of 1100 and 350 °C, respectively. Note that the composition of the source materials was not identical to the aiming I-CFO and C-CFO films because the amounts of oxygen and cation vacancies are expected to be controlled by the film growth conditions.

The PLD was performed using a frequency-doubled Nd : YAG laser with a pulse width of 6 ns and a repetition rate of 30 Hz. The energy density of the laser beam was controlled to 1 J/cm^2 by an optical lens. The I-CFO films were grown in O_2 pressure of 6 Pa at the substrate temperature of 300 °C. The C-CFO films were grown in Ar pressure of 4 Pa at the substrate temperature of 300 °C. The gas pressure conditions and substrate temperatures during the deposition were optimized to obtain CFO films having large in-plane tensile strain in the (001) crystal orientation, which induces PMA. The eclipse PLD method, where a shadow mask was placed between the source material and the substrates, was used to reduce the formation of droplets and particulates [44].

The crystal structures of the prepared films were investigated by x-ray diffraction (XRD) using a Cu-$K\alpha$ source. To investigate the in-plane and out-of-plane strains, reciprocal space maps of XRD intensity were measured for both I-CFO and C-CFO films. The transport properties of prepared films were investigated using the four-probe methods with cooling by a helium cryostat. The MH curves were measured using a superconducting quantum interference device (SQUID) magnetometer. For non-^{57}Fe-enriched films, MS using a radioactive ^{57}Co source was conducted at room temperature (RT) by the conversion electron detection method. The γ rays were irradiated from the film normal direction, and the emitted electrons were detected by a proportional gas counter. X-ray absorption spectroscopy (XAS) and XMCD were performed at BL-7A in the Photon Factory at the High Energy Accelerator Research Organization (KEK-PF). For the XAS and XMCD measurements, the photon helicity was fixed, and a magnetic field of ± 1.2 T was applied parallel along the incident polarized soft x-ray beam, to obtain signals defined as $\mu+$ and $\mu-$ spectra. The total electron yield (TEY) mode was adopted, and all measurements were performed at RT. Since TEY measurements are surface sensitive which detects the signals beneath 3 nm from the sample surface, we prepared the samples for XAS and XMCD by capping the surfaces by 1-nm-thick Pd layers deposited at RT.

III. RESULTS

A. XRD

Figure 1(a) shows the XRD patterns of the typical I-CFO and C-CFO films with various Co compositions ($x = 0.00, 0.23, 0.36$, and 0.66; and $y = 0.00, 0.23, 0.42$, and 0.66), with the scattering vector perpendicular to the film plane. They exhibit clear I-CFO (008) and C-CFO (008) diffraction peaks. This means that the I-CFO and C-CFO films are highly oriented along the [001] directions on MgO (001) substrates. The I-CFO (008) peaks are shifted to lower angles systematically with increasing x, indicating the extension of the lattice along the c axis. On the other hand, the C-CFO (008) peaks are shifted to higher angles systematically with increasing y, indicating the suppression of the lattice along the c axis. The additional satellite peaks, which originate from the interference effect, are detected beside the (008) peaks, showing high-crystalline qualities of the films prepared by PLD with a shadow mask. Figure 1(b) shows the Co composition dependence of the vertical lattice constant $a_\perp$ of the I-CFO and C-CFO films estimated from the XRD patterns. The red and blue broken lines represent the linear relations in Begard law between bulk Fe_3O_4 and $CoFe_2O_4$ and that between bulk γ-Fe_2O_3 and $CoFe_2O_4$, respectively. The out-of-plane lattice constants of the I-CFO films decrease with the decrease of the Co composition x, while those of the C-CFO films increase with the decrease of the Co composition y. Figure 1(c) shows the reciprocal space maps around the MgO (113) peak in the horizontal Q (110) and vertical Q (001) directions for the I-CFO ($x = 0.66$) and C-CFO ($y = 0.66$) films. The I-CFO (226) and C-CFO (226) peaks were observed near the MgO
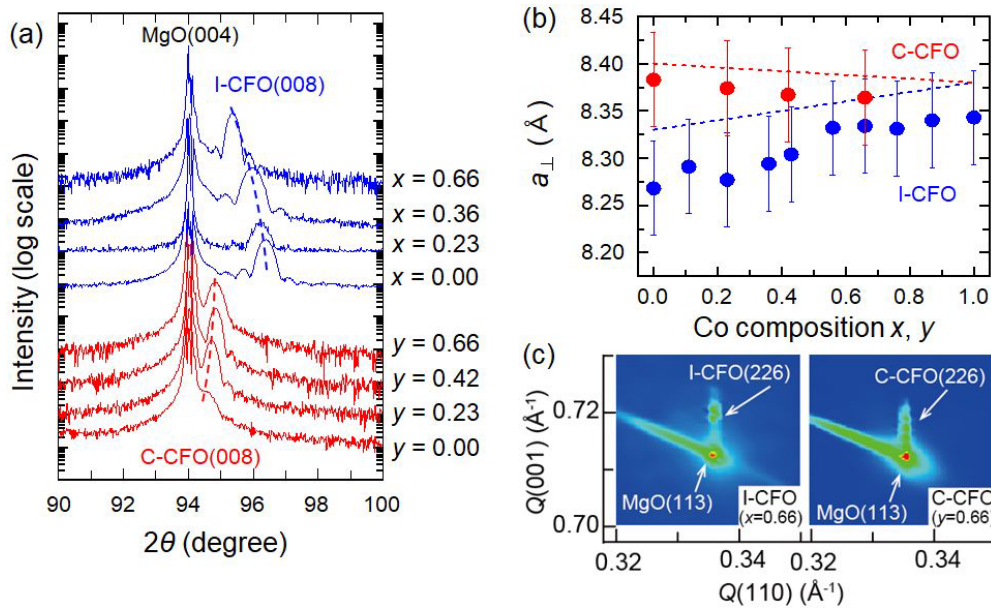
FIG. 1. (a) X-ray diffraction (XRD) patterns around the CFO(008) for the insulative $Co_xFe_{3-x}O_{4+\delta}$ (I-CFO) and conductive $Co_yFe_{3-y}O_4$ (C-CFO) films with the scattering vector perpendicular to the film plane. (b) Vertical lattice constants $\boldsymbol{a}_\perp$ of the I-CFO and C-CFO films as functions of the Co composition x and y. Red and blue broken lines represent the linear relations in Begard law between bulk Fe_3O_4 and $CoFe_2O_4$ and that between bulk γ-Fe_2O_3 and $CoFe_2O_4$, respectively. (c) Reciprocal space maps around the MgO(113) peaks for the I-CFO ($x = 0.66$) and C-CFO ($y = 0.66$) films.

(113) peak. The in-plane Q values of the I-CFO (226) and C-CFO (226) peaks coincide with the value of the MgO (113) peak, which means that the in-plane lattice constants of the I-CFO and C-CFO films are twice that of the MgO substrates (8.42 Å). Note that the tendency of the in-plane lattice constant, which is less dependent on the Co composition, is consistent with previously reported results [19,35]. From the results of the in-plane $a_{||}$ and out-of-plane $a_\perp$ lattice constants, it is suggested that the I-CFO and C-CFO films have in-plane tensile strain and that the structures are tetragonally distorted to settle the lattice mismatch with the MgO substrates.

B. Resistivity measurements

Temperature dependence of resistivity for the C-CFO films grown on MgO (001) substrates with different Co composition y is shown in Fig. 2(a). With increasing y, the resistivity of the C-CFO films systematically increases. For the I-CFO films, the resistivity was $>10^5$ Ω cm at 300 K for all Co compositions x, and they can be regarded as insulators. The resistivity of the C-CFO ($y = 0.00$), Fe_3O_4, film at 300 K is 0.03 Ω cm, which is in the same order as in the previous studies [36,45]. To confirm the hopping conduction through the thermal activation, temperature T dependence of the resistivity ρ is plotted by the Arrhenius equation $\rho = \rho_0 \exp(\Delta E/k_B T)$ and fitted with the least-squares method, as shown in Figs. 2(b)–2(e). Here, ρ_0 is the pre-exponential factor of the resistivity, ΔE is the activation energy, and k_B is the Boltzmann constant. Except the low-temperature parts for $y = 0.00$ and 0.23, the resistivity follows the Arrhenius plots, which means that the conduction mechanism of C-CFO is due to the electron hopping between the B-site Fe ions with different valences. The deviation of the experimental data from the fitting line for

$y = 0.00$ and 0.23 originates from the Verwey transition. The Verwey transition is a dramatic change in the electrical transport properties accompanied with a structural transition from the cubic to the monoclinic phase $\sim$120 K, which suggests that a high-quality Fe_3O_4 film is prepared [46,47]. Figures 2(f) and 2(g) exhibit the composition y dependence of ρ_0 and ΔE, respectively. Here, ΔE corresponds to the activation energy of electron hopping between Fe^{2+} and Fe^{3+} ions. The increase in resistivity with increasing Co in Fig. 2(a) is found to be due to the increase in activation energy of the electron hopping.

C. Magnetic properties

Figures 3(a)–3(d) show the results of magnetization measurements by a SQUID magnetometer with the magnetic field applied along the in-plane and out-of-plane directions at 300 K for the I-CFO ($x = 0.00$, 0.43, and 0.87) and C-CFO ($y = 0.23$, 0.42, and 0.66) films. PMA characteristics are obtained for all cases of the I-CFO and C-CFO films except $x = 0.00$ (γ-Fe_2O_3) and $y = 0.00$ (Fe_3O_4). Figure 3(e) shows the Co composition x, y dependence of squareness ratio M_r/M_s of I-CFO [33] and C-CFO in the out-of-plane MH curves. The squareness ratio in I-CFO is larger than that in C-CFO for the entire Co composition ranges. In I-CFO films, the squareness ratio decreases with the Co composition x. For C-CFO films, on the other hand, the squareness ratio increases with Co composition y. The difference in tendency on the squareness ratio as a function of Co composition can be explained by the strain magnitude as a function of Co composition. As shown in Fig. 1(b), the out-of-plane lattice constants of I-CFO films increase, and those of I-CFO films decrease with the increase of Co composition. The in-plane lattice constants of both I-CFO and C-CFO films almost remain unchanged
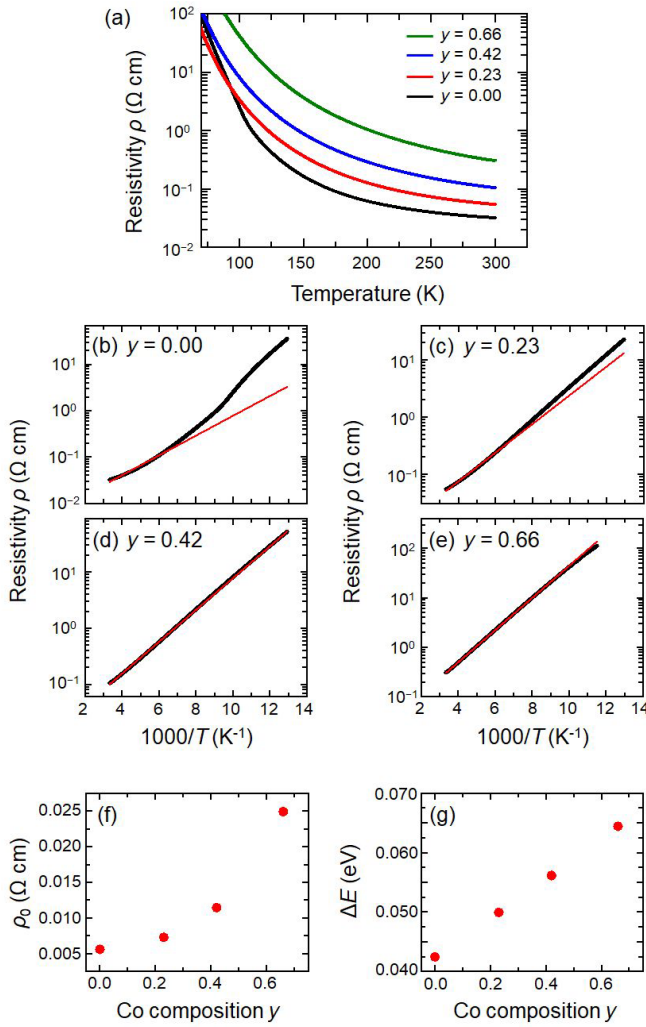
FIG. 2. (a) Electrical resistivity as a function of temperature for conductive $Co_yFe_{3-y}O_4$ films. (b)–(e) Plot of $\log_{10}\rho$ vs $1/T$ with a linear fitting. (f) and (g) Pre-exponential factor of the resistivity ρ_0 and activation energy ΔE as a function of Co composition y.

FIG. 3. Out-of-plane and in-plane magnetic hysteresis (MH) curves at 300 K of the insulative $Co_xFe_{3-x}O_{4+\delta}$ film: (a) $x = 0.00$, (b) $x = 0.43$, and (c) $x = 0.87$; and the conductive $Co_yFe_{3-y}O_4$ film: (d) $y = 0.23$, (e) $y = 0.42$, and (f) $y = 0.66$. (g) Squareness ratio of remanent and saturation magnetizations M_r/M_s as a function of Co composition for I-CFO and C-CFO films.

for all Co compositions. Therefore, the distortion of I-CFO films decreases, and that of C-CFO films increases with the Co composition x. The PMA energies estimated from the area surrounded by the loops of out-of-plane and in-plane loops for I-CFO ($x = 0.66$) and C-CFO ($y = 0.66$) are 1.0 and 0.3 MJ/m^3, respectively. The deterioration of the squareness in the MH curves and the changes of M_s imply the existence of APB in the films.

D. Mössbauer spectroscopy

Figure 4 shows the ^{57}Fe Mössbauer spectra for the I-CFO ($x = 0.23$) and C-CFO ($y = 0.23$) films taken at RT using the conversion electron Mössbauer spectrometry mode. Both cases clearly show magnetic spectra, with no component from α-Fe or α-Fe$_2$O$_3$. In the case of I-CFO, a six-line spectrum pattern with symmetric line heights is observed, which suggests that the film is composed only of Fe^{3+} ions without Fe^{2+} ions. This is consistent with the resistivity measurement because the hopping conduction is suppressed without Fe^{2+}
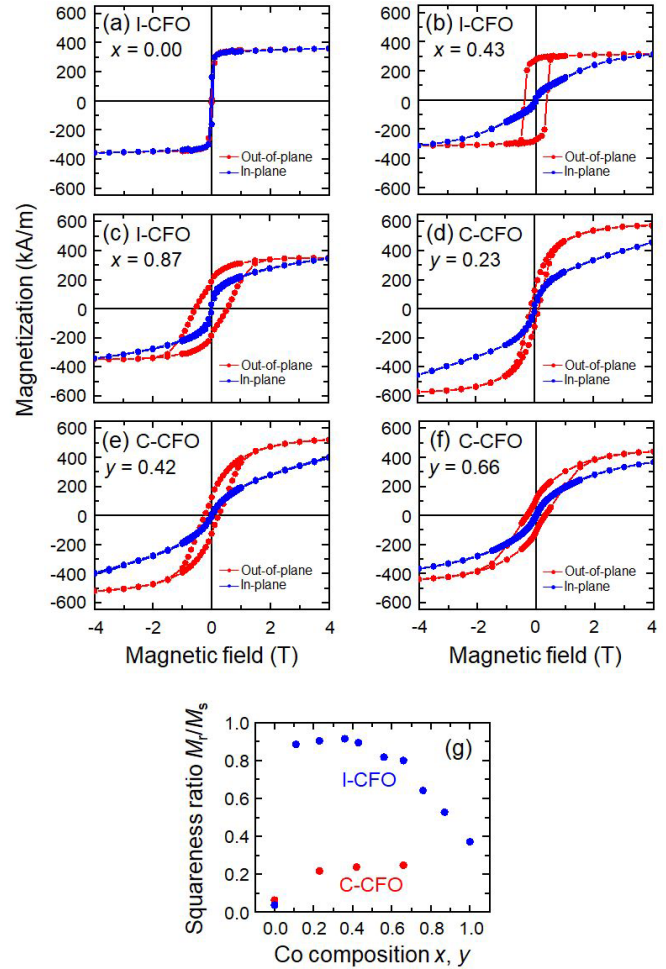
[48–50]. On the other hand, the spectrum for C-CFO represents an asymmetric and rather broad line shape due to the overlapping of two magnetic components. These spectra are fitted using the Mössbauer parameters of isomer shift (δ), quadrupole shift (2ε), and hyperfine field (B_{hf}). The fitted parameters are listed in Table I. For C-CFO, two kinds of magnetic components corresponding to the A- and B-sites in the spinel structure are necessary for the fitting. The B-site components are detected as an Fe$^{2.5+}$ sextet because the observation time in MS is longer than the time scale of electron hopping between Fe^{3+} and Fe^{2+} sites. The combination of two magnetic components with different isomer shift and hyperfine fields clearly reproduce the asymmetric spectra. The obtained Mössbauer parameters are like those in the previous reports on Mössbauer spectra of CoFe$_2$O$_4$ [2,7,10,12,51,52] and Fe$_3$O$_4$ [53,54]. From these site-specific analyses, the Fe^{2+} components are thought to be essential for the conductivity in C-CFO.

The intensity ratios of the six lines in both spectra are between 3:0:1:1:0:3 and 3:2:1:1:2:3, which means that the
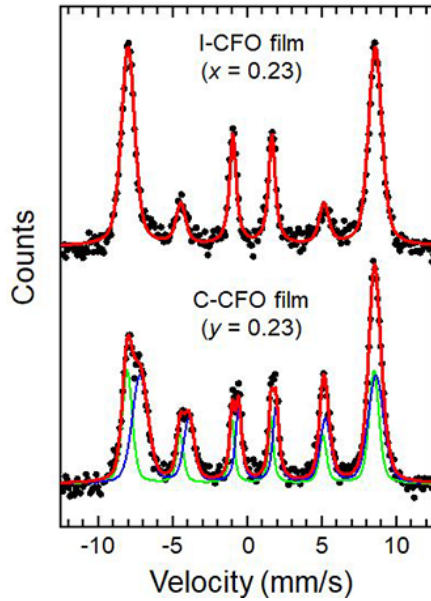
FIG. 4. Mössbauer spectra for insulative $Co_{0.23}Fe_{2.77}O_{4+\delta}$ (I-CFO) and conductive $Co_{0.23}Fe_{2.77}O_4$ (C-CFO) films taken at room temperature (RT). Dots represent the experimental data. Lines are fitting results. For C-CFO, two components (green line for A-site, blue line for B-site) are used, and the sum of these are also shown.

films have PMA but that the direction of the magnetic moment is not perfectly perpendicular to the film plane at zero external field. This is consistent with the magnetization measurements, where the squareness ratios do not reach 1. The intensity ratio of the second and fifth peaks is smaller for the I-CFO film, suggesting that the perpendicular anisotropy is stronger in the I-CFO system.

E. XAS and XMCD

Figure 5 shows the XAS and XMCD of C-CFO for Fe and Co L-edges with different Co compositions. Spectra are normalized by an incident white line beam intensity before the absorption at the samples. The Fe and Co intensities are plotted in the same vertical scales because XAS roughly provides the Fe and Co compositions. Because of the composition ratio of Co : Fe = 1 : 12 in $y = 0.23$, the XAS intensities of Co in this film are suppressed. With increasing the Co compositions, the Co L-edge intensities are enhanced systematically. XAS and XMCD line shapes for the Fe L-edges show distinctive features with differential line shapes due to the three kinds of Fe states (Fe^{3+} in O_h, Fe^{3+} in T_d, and Fe^{2+} in O_h). For the Fe
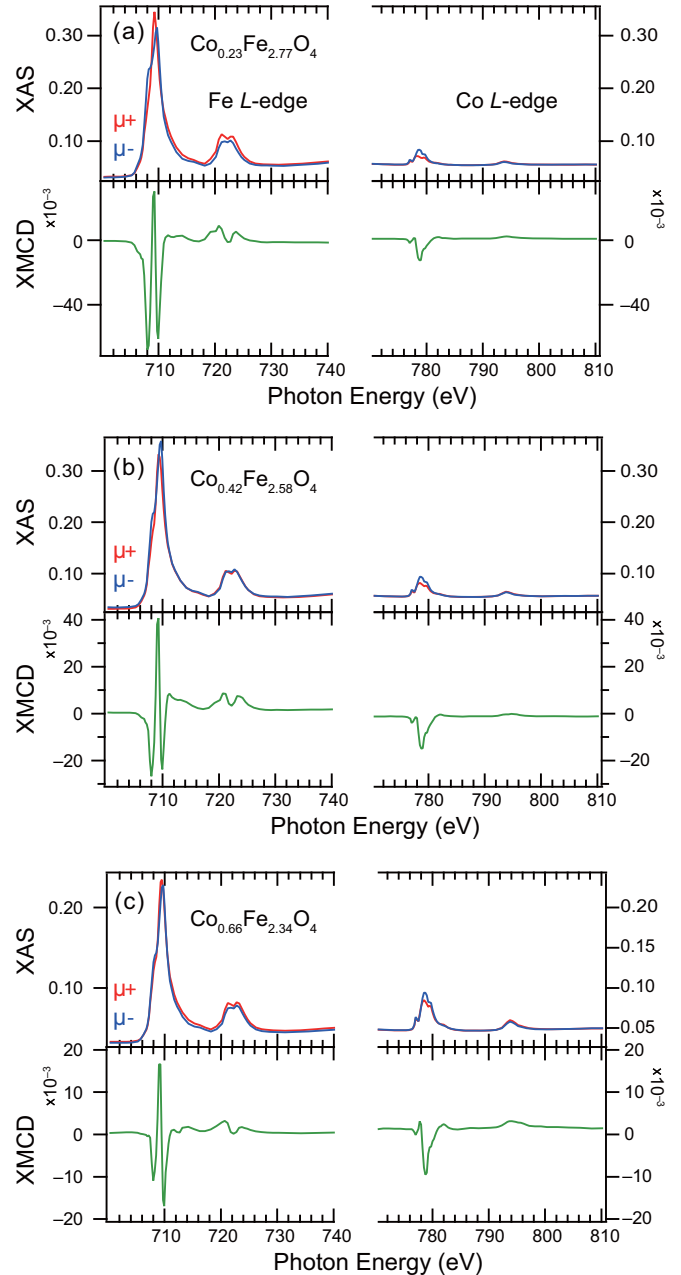

FIG. 5. X-ray absorption spectroscopy (XAS) and x-ray magnetic circular dichroism (XMCD) of conductive $Co_yFe_{3-y}O_4$ films for $y = 0.23$, 0.42, and 0.66.

L-edges, although the difference in XAS is small, clear differential XMCD line shapes are detected. The Fe^{3+} state with T_d symmetry exhibits the opposite XMCD sign, which is common for the spinel ferrite compounds. The Fe^{2+} component at 708.0 eV decreases in high Co compositions. In the case of Fe_3O_4, the Fe^{2+} component is more enhanced [38]. Therefore, the conductive properties are related to the amounts of Fe^{2+} states, whose quantitative analysis is performed by using the ligand-field-multiplet (LFM) calculation later. The cases of I-CFO are also shown in Fig. 6, which is like the previous reports [35]. Large XMCD signals in Co L-edge despite small XAS intensity correspond to the saturated magnetized states.

TABLE I. Mössbauer fitting parameters for I-CFO and C-CFO films. Isomer shifts (δ) were defined with respect to α-Fe at RT.

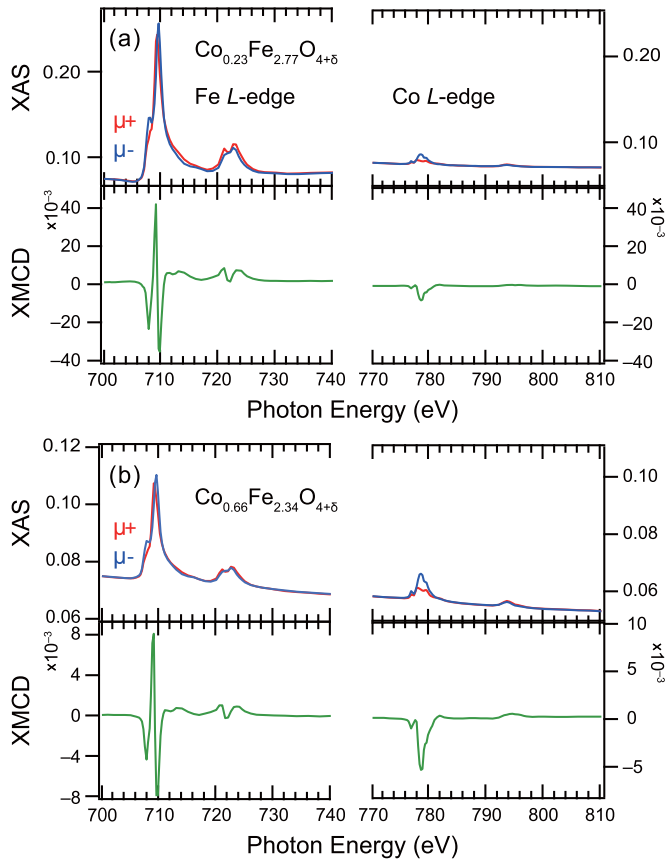| Sample	Subspectra	δ (mm/s)	2ε (mm/s)	B_{hf} (T)	Area (%)
I-CFO	Fe^{3+}	0.33	−0.06	51.4	
C-CFO	Fe^{3+} A-site	0.26	−0.06	51.4	39.8
	$Fe^{2.5+}$ B-site	0.70	0.05	49.1	60.2

FIG. 6. X-ray absorption spectroscopy (XAS) and x-ray magnetic circular dichroism (XMCD) of insulative $Co_xFe_{3-x}O_{4+\delta}$ films for $x = 0.23$ and 0.66.

FIG. 7. Ligand-field-multiplet (LFM) cluster-model calculation of Fe^{2+} and Fe^{3+} states. (a) Fragments of O_h and T_d symmetries used in the calculation drawn by VESTA [57]. (b) Calculated x-ray magnetic circular dichroism (XMCD) spectra of Fe^{3+} (O_h, T_d) and Fe^{2+} (O_h). (c) and (d) XMCD spectra of experimental (dots) and LFM calculation (lines) for $y = 0.23$ and 0.66.

Within the orbital sum rule, the large orbital magnetic moments (m_{orb}) come from the asymmetric XMCD line shapes. Since the Co site is almost identified as Co^{2+} (O_h) symmetry, the sum rules can be applicable for the Co XMCD spectra. We note that the sum rule analysis for the entire Fe L-edge XMCD cannot be applicable because it includes three kinds of components, which has to be deconvoluted into each component because XAS/XMCD originates from the atomic excitation process [55]. The spin and orbital magnetic moments for Co^{2+} sites in the $y = 0.23$ sample are estimated as 1.32 and 0.63 μ_B, respectively, using an electron number of 7.1 [33]. Large m_{orb} originates from the orbital degeneracy in the d^7 electron system in strained Co sites and contributes to PMA [56]. The strained Co sites are also confirmed by the extended x-ray absorption fine structures [35].

For the analysis of XMCD spectra, we employed the LFM cluster-model calculations including the configuration interaction for the Fe sites in $Co_yFe_{3-y}O_4$ of $y = 0.23$ and 0.66 as tetrahedral (T_d) TMO_4 and octahedral (O_h) TMO_6 clusters, modeled as a fragment of the spinel-type structures. The line shapes of Fe^{2+} (O_h), Fe^{3+} (O_h), and Fe^{3+} (T_d) are calculated in the previous reports in I-CFO using the Coulomb interaction U of 6.0 eV [35] by considering the chemical shift of energy position through the electron number. Here, we adopt this analysis for the estimations of the ratio in Fe^{2+} and Fe^{3+} intensities.
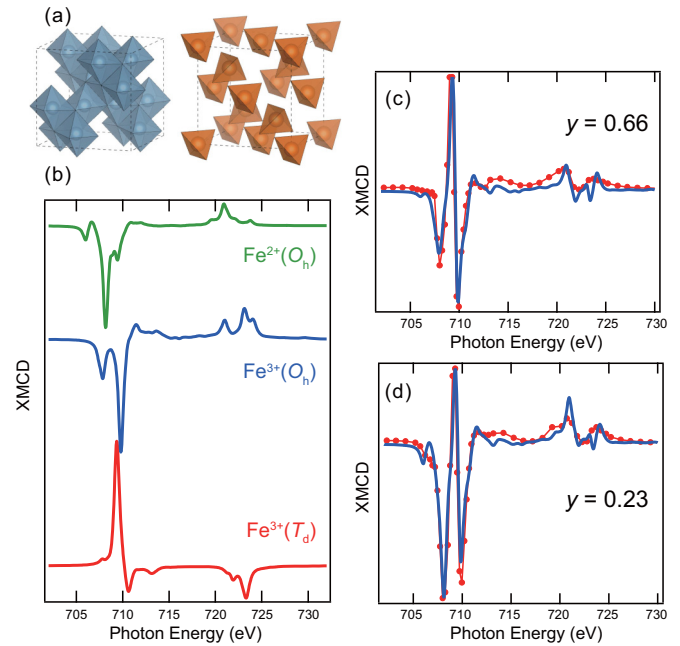
As shown in Fig. 7, the spectral line shapes of XMCD can be reproduced by the LFM calculations qualitatively, at least the peak positions, with three kinds of Fe states. The XMCD spectra for different valences and symmetries are calculated by using the same parameters as the cases of I-CFO [35]. The peak position of Fe^{2+} (709.0 eV) is composed of not only Fe^{2+} but also Fe^{3+} (O_h) contribution. We fitted the spectra using these LFM-calculated spectra by changing the ratios of three components. Then the ratios of Fe^{2+} (O_h), Fe^{3+} (O_h), and Fe^{3+} (T_d) can be estimated to be 1:1:1 for $y = 0.23$ and 0.2:1:1 for $y = 0.66$. The fitting results indicate that the intensity ratio of Fe^{3+} (O_h) and Fe^{3+} (T_d) is not affected by the Co ion substitution. Therefore, the site-specific analysis in XMCD clearly deduces the contributions of Fe^{2+} states, although it might be overestimated, which play an essential role for the conduction mechanism in C-CFO films.

F. DFT calculation

To investigate the conductive properties of $Co_yFe_{3-y}O_4$ films from the viewpoint of the electronic structures, we performed first-principles density functional theory (DFT) calculations with periodic boundary conditions for an optimized $Co_1Fe_{11}O_{16}$ supercell structure shown in Fig. 8(a), which was considered as the C-CFO of $Co_{0.25}Fe_{2.75}O_4$ ($y = 0.25$). The lattice constant for the unit cell of 8.35 Å was employed which includes the strain estimated from the XRD experiments. The unit cell includes the A- and B-sites of 4 and 8 cations, respectively, and these correspond to 4 Fe^{3+} ions at the A-sites, and 4 Fe^{3+} ions, 3 Fe^{2+} ions, and 1 Co^{2+} ions at the B-sites. The DFT calculations were performed using
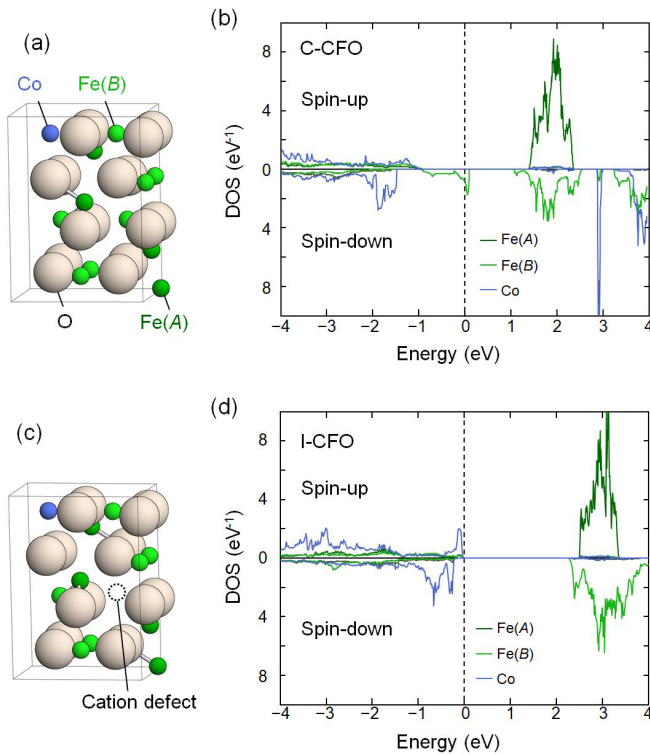
FIG. 8. (a) Crystal structure of the conductive $Co_1Fe_{11}O_{16}$ (C-CFO) used in first-principles calculation. The white, dark green, light green, and blue spheres are O, Fe (A-site), Fe (B-site), and Co atoms, respectively. (b) The local density of states (DOS) for $Co_1Fe_{11}O_{16}$ of spin-up and spin-down states. The Fermi energy was set to 0 eV. (c) Crystal structure of insulative $Co_1Fe_{10}O_{16}$ (I-CFO) used in first-principles calculation. The white, dark green, light green, and blue spheres are O, Fe (A-site), Fe (B-site), and Co atoms, respectively. The dotted circle represents a cation defect. (d) The local DOS for $Co_1Fe_{10}O_{16}$ spin-up and spin-down states.

the VASP code with the projector augmented-wave potentials [58] in the generalized gradient approximation Perdew-Burke-Ernzerhof [59,60], including the Coulomb repulsion energy U of 6.0 eV. The cutoff energy is set to 400 eV, and the crystal momentum k sampling mesh is set to (21, 21, 17).

Figure 8(b) shows the calculated spin-dependent density of states (DOS) for $Co_1Fe_{11}O_{16}$ as C-CFO. The spin-down states of the B-site in Fe cross the Fermi level (E_F) and contribute to the conductivity. The partial DOS of the Co site is located at a deeper level and does not contribute to the formation of the intensity at the E_F. The band gap between occupied and unoccupied spin-up states is estimated to be 2.58 eV. The DOS clearly indicates a half-metallic property. The Fe magnetic moment of -4.15 μ_B for A-sites and 4.02 μ_B for B-sites can be estimated. The local magnetic moment of 2.70 μ_B of the Co site is also estimated, which is smaller than those of Fe sites and qualitatively consistent with that of the XMCD analysis.

We also calculated the spin-dependent DOS for an optimized $Co_1Fe_{10}O_{16}$ supercell structure, as shown in Fig. 8(c), which is considered as the I-CFO of $Co_{0.25}Fe_{2.50}O_4$ or $Co_{0.273}Fe_{2.727}O_{4.364}$ ($x = 0.273$, $\delta = 0.364$). The calculated DOS is shown in Fig. 8(d), and the insulating property can be seen. The band gaps between occupied and unoccupied states

in spin-up and spin-down cases are estimated to be 2.67 and 2.40 eV, respectively, whose entire DOS is like the previous results of I-CFO [33]. Note that this spin-dependent difference in the band gaps can be applied for the generation of the spin-polarized electrons. In fact, we reported that electrons tunneling through the I-CFO thin films were spin polarized because of the difference in tunnel probability of spin-up and spin-down electrons caused by the difference in the band gaps [19]. The half-metallic property is guaranteed in the C-CFO, as in the case of Fe_3O_4, where B-site DOS contributes the conduction at the E_F [38].

IV. DISCUSSION

The conduction mechanism, structural deformation, and advantages in I-CFO and C-CFO can be discussed using the above results. First, MS and XMCD reveal the existence of Fe^{2+} states in C-CFO, which is responsible for the conduction as analogous to the case of Fe_3O_4. However, for I-CFO, small amounts of Fe^{2+} states are still detected in XMCD, which is not detected in MS, as shown in Fig. 4. It may come from the difference in probing regions; while the MS detects the bulk information because of the larger escape depth of the conversion electrons (∼100 nm) in comparison with the film thickness (20 nm), XMCD in soft x-ray detects the surface regions beneath 3 nm from the sample surface since the valence states of surface regions are slightly modulated and the surface oxygen reduction might occur. However, it is not significant but an offset factor for the detailed analysis of Fe^{2+} states to estimate the chemical compositions. Therefore, site-specific magnetic spectroscopies by MS and XMCD provide complementary information for the analyses of I-CFO and C-CFO.

Second, the conduction mechanism can be discussed by combining the resistivity and DFT calculations. As an analogous system with Fe_3O_4, the conduction in C-CFO is caused by the electron hopping between Fe^{2+} and Fe^{3+} in the B-site through the activation-type excitation. Temperature dependence of the resistivity in Fig. 2 is different from the small polaron formation and variable range hopping schemes [48]. The double-exchange mechanism can be anticipated in the t_{2g} states. The half-metallic nature in the DFT calculations can also be explained by the electron hopping mechanism, which is different from the noble metals and distinctive for conductive oxide materials such as perovskite Mn oxide compounds [61]. Yasui et al. [38] reported that a large TMR effect was obtained for Fe_3O_4/MgO/Fe MTJs and that the large TMR effect derives from the half-metallic nature of Fe_3O_4. Thus, the half-metallic C-CFO films may become good candidates for spin injectors in spintronics devices.

Finally, we discuss the selective growth of two types of Fe-rich CFO, C-CFO and I-CFO. The element- and site-selective XMCD and MS clearly suggest the valance states of Fe^{2+} are essential factors for controlling the conductivity of CFO. For the growth of Fe-rich CFO films, the valance states of Fe ions can be controlled by changing the oxygen flow rate, the source materials, and the substrate temperature during the growth with the deposition atmosphere. The depositions under O_2 pressure with high growth temperature promote the oxidation of Fe^{2+} states. On the other hand, the depositions under Ar pressure with low growth temperature suppress the

oxidation of Fe^{2+} states. In the case of C-CFO, the XMCD results (Fig. 7) show that the abundance ratio of Fe^{2+} ions in the *B*-site decreases with increasing the Co composition *y*, which suggests that the Co^{2+} ions in $CoFe_2O_4$ are replaced with Fe^{2+} ions. The XRD results [Fig. 2(b)] also display that the vertical lattice constant of C-CFO films increases with decreasing *y*. From these results, C-CFO can be recognized as a magnetite-type CFO because its bond distances are tuned between $CoFe_2O_4$ and Fe_3O_4 according to the *y* values, qualitatively following the Begard law. On the other hand, in the case of I-CFO, the XRD result shows that the vertical lattice constant of I-CFO films decreases with decreasing *y* [33]. Therefore, I-CFO can be considered a maghemite-type CFO because of the tuning of $CoFe_2O_4$ and γ-Fe_2O_3 compositions according to *x* values. The junction composed of I-CFO tunnel barriers and C-CFO electrode layers can be applicable to spintronics research and demonstrated for the spin-filtering effect with PMA [19].

V. SUMMARY

We fabricated two types of Fe-rich cobalt-ferrite thin films, insulative $Co_xFe_{3-x}O_{4+\delta}$ (I-CFO) and conductive $Co_yFe_{3-y}O_4$ (C-CFO), with PMA. Although the stoichiometric cobalt ferrites are known as insulating materials, it is found

that the conductivity in Fe-rich CFO can be controlled by changing the source materials and deposition conditions in the PLD technique. The I-CFO and C-CFO films also exhibit PMA through the in-plane lattice distortion. We investigated the Fe-ion-specific valence states in I-CFO and C-CFO films by MS and XMCD and found that the difference in conductivity corresponds to the abundance ratio of the Fe^{2+} state at the octahedral (O_h) site. Furthermore, first-principles band-structure calculation suggested that the electronic structures of C-CFO are half-metallic characteristics and reproduced the difference in the DOS depending on the cation vacancies at the *B*-site in inverse spinel structures, which explains the difference in the conductivity between I-CFO and C-CFO. These advantages benefit the oxide spintronics using Fe-rich CFO films.

[1] R. M. Bozorth, E. F. Tilden, and A. J. Williams, Anisotropy and magnetostriction of some ferrites, Phys. Rev. **99**, 1788 (1955).

[2] A. Lisfi, M. Guyot, R. Krishnan, M. Porte, P. Rougier, and V. Cagan, Microstructure and magnetic properties of spinel and hexagonal ferrimagnetic films prepared by pulsed laser deposition, J. Magn. Magn. Mater. **157–158**, 258 (1996).

[3] M. Grigorova, H. J. Blythe, V. Blaskov, V. Rusanov, V. Petkov, V. Masheva, D. Nihtianova, Ll. M. Martinez, J. S. Muñoz, and M. Mikhov, Magnetic properties and Mössbauer spectra of nanosized $CoFe_2O_4$ powders, J. Magn. Magn. Mater. **183**, 163 (1998).

[4] J. A. Moyer, C. A. F. Vaz, E. Negusse, D. A. Arena, and V. E. Henrich, Controlling the electronic structure of $Co_{1-x}Fe_{2+x}O_4$ thin films through iron doping, Phys. Rev. B **83**, 035121 (2011).

[5] M. Foerster, M. Iliev, N. Dix, X. Marti, M. Barchuk, F. Sanchez, and J. Fontcuberta, The poisson ratio in $CoFe_2O_4$ spinel thin films, Adv. Funct. Mater. **22**, 4344 (2012).

[6] R. C. Rai, S. Wilser, M. Guminiak, B. Cai, and M. L. Nakarmi, Optical and electronic properties of $NiFe_2O_4$ and $CoFe_2O_4$ thin films, Appl. Phys. A: Mater. Sci. Process. **106**, 207 (2012).

[7] J. de la Figuera, A. Quesada, L. MartÌn-GarcÌa, M. Sanz, M. Oujja, M. Castillejo, A. Mascaraque, A. T. N'Diaye, M. Foerster, L. Aballe *et al.*, Mössbauer and magnetic properties of coherently mixed magnetite-cobalt ferrite grown by infrared pulsed-laser deposition, Croatica Quimica Acta **88**, 453 (2015).

[8] M. Scigaj, N. Dix, J. Gazquez, M. Varela, I. Fina, N. Domingo, G. Herranz, V. Skumryev, J. Fontcuberta, and F. Sanchez, Monolithic integration of room temperature multifunctional $BaTiO_3$-$CoFe_2O_4$ epitaxial heterostructures on Si(001), Sci. Rep. **6**, 31870 (2016).

[9] S. E. Shirsath, X. Liu, Y. Yasukawa, S. Li, and A. Morisako, Switching of magnetic easy-axis using crystal orientation for large perpendicular coercivity in $CoFe_2O_4$ thin film, Sci. Rep. **6**, 30074 (2016).

[10] M. Liu, M. Lu, L. Wang, S. Xu, J. Zhao, and H. Li, Mössbauer study on the magnetic properties and cation distribution of $CoFe_2O_4$ nanoparticles synthesized by hydrothermal method, J. Mater. Sci. **51**, 5487 (2016).

[11] S. Y. Huang, C.-W. Chong, Y. Tung, T.-C. Chen, K.-C. Wu, M.-K. Lee, J.-C.-A. Huang, Z. Li, and H. Qiu, Proximity effect induced transport properties between MBE grown $(Bi_{1-x}Sb_x)_2Se_3$ topological insulators and magnetic insulator $CoFe_2O_4$, Sci. Rep. **7**, 2422 (2017).

[12] M. Al-Maashani, A. M. Gismelseed, K. A. M. Khalaf, Ali A. Yousif, A. D. Al-Rawas, H. M. Widatallah, and M. E. Elzain, Structural and Mössbauer study of nanoparticles $CoFe_2O_4$ prepared by sol-gel auto-combustion and subsequent sintering, Hyperfine Interact. **239**, 15 (2018).

[13] K. Prabahar, R. Ranjith, P. Saravanana, and A. Srinivasa, Effect of magnetic field annealing on the magnetostriction and deflection properties of $CoFe_2O_4$ thin films grown by PLD, J. Magn. Magn. Mater. **475**, 276 (2019).

[14] M. G. Chapline and S. X. Wang, Room-temperature spin filtering in a $CoFe_2O_4$ /$MgAl_2O_4$ /Fe_3O_4 magnetic tunnel barrier, Phys. Rev. B **74**, 014418 (2006).

[15] A. V. Ramos, M.-J. Guittet, J.-B. Moussy, R. Mattana, C. Deranlot, F. Petroff, and C. Gatel, Room temperature spin filtering in epitaxial cobalt-ferrite tunnel barriers, Appl. Phys. Lett. **91**, 122107 (2007).

[16] K. Inomata, N. Ikeda, N. Tezuka, R. Goto, S. Sugimoto, M. Wojcik, and E. Jedryka, Highly spin-polarized materials and devices for spintronics, Sci. Technol. Adv. Mater. **9**, 014101 (2008).

[17] Y. K. Takahashi, S. Kasai, T. Furubayashi, S. Mitani, K. Inomata, and K. Hono, High spin-filter efficiency in a Co ferrite fabricated by a thermal oxidation, Appl. Phys. Lett. **96**, 072512 (2010).

[18] N. M. Caffrey, D. Fritsch, T. Archer, S. Sanvito, and C. Ederer, Spin-filtering efficiency of ferrimagnetic spinels $CoFe_2O_4$ and $NiFe_2O_4$, Phys. Rev. B **87**, 024419 (2013).

[19] M. Tanaka, Furuta M, T. Ichikawa, M. Morishita, Y. Hung, S. Honda, T. Ono, and K. Mibu, Generation of spin-polarized electronic currents using perpendicularly magnetized cobalt-ferrite spin-filtering barriers grown on spinel-type-conductive layers, Appl. Phys. Lett. **122**, 042401 (2023).

[20] P. C. Dorsey, P. Lubitz, D. B. Chrisey, and J. S. Horwitz, $CoFe_2O_4$ thin films grown on (100) MgO substrates using pulsed laser deposition, J. Appl. Phys. **79**, 6338 (1996).

[21] N. Hiratsuka, M. Nozawa, and K. Kakizaki, Magnetic properties of cobalt ferrite films with perpendicular magnetic anisotropy, J. Magn. Magn. Mater. **176**, 31 (1997).

[22] Y. Suzuki, G. Hu, R. B. van Dover, and R. J. Cava, Magnetic anisotropy of epitaxial cobalt ferrite thin films, J. Magn. Magn. Mater. **191**, 1 (1999).

[23] S. Chambers, R. Farrow, S. Maat, M. Toney, L. Folks, J. Catalano, T. Trainor, and G. Brown, Molecular beam epitaxial growth and properties of $CoFe_2O_4$ on MgO (001), J. Magn. Magn. Mater. **246**, 124 (2002).

[24] A. Lisfi, C. M. Williams, L. T. Nguyen, J. C. Lodder, A. Coleman, H. Corcoran, A. Johnson, P. Chang, A. Kumar, and W. Morgan, Reorientation of magnetic anisotropy in epitaxial cobalt ferrite thin films, Phys. Rev. B **76**, 054405 (2007).

[25] J. A. Moyer, C. A. F. Vaz, D. A. Arena, D. Kumah, E. Negusse, and V. E. Henrich, Magnetic structure of Fe-doped $CoFe_2O_4$ probed by x-ray magnetic spectroscopies, Phys. Rev. B **84**, 054447 (2011).

[26] H. Yanagihara, K. Uwabo, M. Minagawa, E. Kita, and N. Hirota, Perpendicular magnetic anisotropy in epitaxially strained cobalt-ferrite (001) thin films, J. Appl. Phys. **109**, 07C122 (2011).

[27] R. Comes, M. Gu, M. Khokhlov, J. Lu, and S. A. Wolf, Magnetic anisotropy in composite $CoFe_2O_4$-$BiFeO_3$ ultrathin films grown by pulsed laser deposition, J. Magn. Magn. Mater. **324**, 524 (2012).

[28] T. Niizeki, Y. Utsumi, R. Aoyama, H. Yanagihara, J. Inoue, Y. Yamasaki, H. Nakao, K. Koike, and E. Kita, Extraordinarily large perpendicular magnetic anisotropy in epitaxially strained cobalt-ferrite $Co_xFe_{3-x}O_4(001)$ ($x = 0.75$, 1.0) thin films, Appl. Phys. Lett. **103**, 162407 (2013).

[29] M. A. Tanaka, K. Harada, M. Takemura, K. Mibu, and J. Inoue, Nonlinear strain dependence of magnetic anisotropy in $CoFe_2O_4$ films on MgO(001) substrates, J. Appl. Phys. **115**, 17C101 (2014).

[30] J. Inoue, H. Yanagihara, and E. Kita, Magnetic anisotropy and magnetostriction in cobalt-ferrite with lattice deformation, Mater. Res. Express **1**, 046106 (2014).

[31] Y. Zhang, L. Shen, M. Liu, X. Li, X. Lu, L. Lu, C. Ma, C. You, A. Chen, C. Huang *et al.*, Flexible quasi-two-dimensional $CoFe_2O_4$ epitaxial thin films for continuous strain tuning of magnetic properties, ACS Nano **11**, 8002 (2017).

[32] T. Tainosho, J. Inoue, S. Sharmin, M. Takeguchi, E. Kita, and H. Yanagihara, Large negative uniaxial magnetic anisotropy in highly distorted Co-ferrite thin films, Appl. Phys. Lett. **114**, 092408 (2019).

[33] K. Naruse, M. A. Tanaka, K. Nomura, T. Taniguchi, S. Honda, T. Ono, and K. Mibu, Perpendicular magnetic anisotropy and tunneling conductivity of epitaxial cobalt-ferrite (001) films grown on nonmagnetic metal films, J. Magn. Magn. Mater. **475**, 721 (2019).

[34] H. Onoda, H. Sukegawa, J.-I. Inoue, and H. Yanagihara, Strain engineering of magnetic anisotropy in epitaxial films of cobalt ferrite, Adv. Mater. Interfaces **8**, 2101034 (2021).

[35] J. Okabayashi, M. A. Tanaka, M. Morishita, H. Yanagihara, and K. Mibu, Origin of perpendicular magnetic anisotropy in $Co_xFe_{3-x}O_{4+\delta}$ thin films studied by x-ray magnetic circular and linear dichroisms, Phys. Rev. B **105**, 134416 (2022).

[36] M. Takahashi, T. Ohshima, H. Yamahara, M. Seki, and H. Tabata, Highly spin-polarized current in Co-substituted Fe_3O_4 epitaxial thin films at room temperature, J. Appl. Phys. **116**, 213907 (2014).

[37] T. Nagahama, Y. Matsuda, K. Tate, T. Kawai, N. Takahashi, S. Hiratani, Y. Watanabe, T. Yanase, and T. Shimada, Magnetic properties of epitaxial Fe_3O_4 films with various crystal orientations and tunnel magnetoresistance effect at room temperature, Appl. Phys. Lett. **105**, 102410 (2014).

[38] S. Yasui, S. Honda, J. Okabayashi, T. Yanase, T. Shimada, and T. Nagahama, Large Inverse Tunnel Magnetoresistance in Magnetic Tunnel Junctions with an Fe_3O_4 Electrode, Phys. Rev. Appl. **15**, 034042 (2021).

[39] D. T. Margulies, F. T. Parker, F. E. Spada, R. S. Goldman, J. Li, R. Sinclair, and A. E. Berkowitz, Anomalous moment and anisotropy behavior in Fe_3O_4 films, Phys. Rev. B **53**, 9175 (1996).

[40] D. T. Margulies, F. T. Parker, M. L. Rudee, F. E. Spada, J. N. Chapman, P. R. Aitchison, and A. E. Berkowitz, Origin of the Anomalous Magnetic Behavior in Single Crystal Fe_3O_4 Films, Phys. Rev. Lett. **79**, 5162 (1997).

[41] S. Celotto, W. Eerenstein, and T. Hibma, Characterization of anti-phase boundaries in epitaxial magnetite films, Eur. Phys. J. B **36**, 271 (2003).

[42] A. V. Singh, B. Khodadadi, J. B. Mohammadi, S. Keshavarz, T. Mewes, D. S. Negi, R. Datta, Z. Galazka, R. Uecker, and A. Gupta, Bulk single crystal-like structural and magnetic characteristics of epitaxial spinel ferrite thin films with elimination of antiphase boundaries, Adv. Mater. (Weinheim) **29**, 1701222 (2017).

[43] Z. Li, J. Lu, L. Jin, J. Rusz, V. Kocevski, H. Yanagihara, E. Kita, J. Mayer, R. E. Dunin-Borkowski, H. Xiang *et al.*, Atomic structure and electron magnetic circular dichroism of individual rock salt structure antiphase boundaries in spinel ferrites, Adv. Funct. Mater. **31**, 2008306 (2021).

[44] H. Nakatsuka, H. Ishibashi, and T. Kobayashi, Dynamics of laser-ablated particles in newly developed eclipse PLD, AIP Conf. Proc. **369**, 1286 (1996).

[45] X. W. Li, A. Gupta, G. Xiao, and G. Q. Gong, Transport and magnetic properties of epitaxial and polycrystalline magnetite thin films, J. Appl. Phys. **83**, 7049 (1998).

[46] G. Q. Gong, A. Gupta, Gang Xiao, W. Qian, and V. P. Dravid, Magnetoresistance and magnetic properties of epitaxial magnetite thin films, Phys. Rev. B **56**, 5096 (1997).

[47] W. Eerenstein, T. T. M. Palstra, T. Hibma, and S. Celotto, Origin of the increased resistivity in epitaxial Fe_3O_4 films, Phys. Rev. B **66**, 201101(R) (2002).

[48] R. Ramos, S. K. Arora, and I. V. Shvets, Anomalous anisotropic magnetoresistance in epitaxial Fe_3O_4 thin films on MgO(001), Phys. Rev. B **78**, 214402 (2008).

[49] A. Fernández-Pacheco, J. Orna, J. M. De Teresa, P. A. Algarabel, L. Morellon, J. A. Pardo, M. R. Ibarra, E. Kampert, and U. Zeitler, High-field Hall effect and magnetoresistance in Fe_3O_4 epitaxial thin films up to 30 Tesla, Appl. Phys. Lett. **95**, 262108 (2009).

[50] N. Naftalis, Y. Shperber, J. A. Moyer, C. H. Ahn, and L. Klein, Thickness dependence of the resistivity tensor in epitaxial magnetite thin films, J. Appl. Phys. **114**, 043701 (2013).

[51] S. J. Kim, S. W. Lee, and C. S. Kim, Mössbauer studies on exchange interactions in $CoFe_2O_4$, Jpn. J. Appl. Phys. **40**, 4897 (2001).

[52] S. V. Bhandare, R. Kumar, A. V. Anupama, H. K. Choudhary, V. M. Jali, and B. Sahoo, Mechanistic insights into the sol-gel synthesis of complex (quaternary) Co–Mn–Zn-spinel ferrites: An annealing dependent study, Ceram. Int. **46**, 17400 (2020).

[53] T. Fujii, M. Takano, R. Katano, Y. Bando, and Y. Isozumi, Depth selective Mössbauer spectroscopic study of Fe_3O_4 epitaxial films, J. Appl. Phys. **68**, 1735 (1990).

[54] H. Yanagihara, M. Myoka, D. Isaka, T. Niizeki, K. Mibu, and E. Kita, Selective growth of Fe_3O_4 and γ-Fe_2O_3 films with reactive magnetron sputtering, J. Phys. D: Appl. Phys. **46**, 175004 (2013).

[55] J. Okabayashi, Tailoring spins and orbitals probed by x-ray magnetic circular dichroism, in *Progress in Photon Science II*, edited by K. Yamanouchi, S. Tunik, and V. Makarov (Springer Nature, Switzerland, 2019), pp. 471–492.

[56] Y. Miura and J. Okabayashi, Understanding magnetocrystalline anisotropy based on orbital and quadrupole moments, J. Phys.: Condens. Matter **34**, 473001 (2022).

[57] K. Momma and F. Izumi, VESTA 3 for three-dimensional visualization of crystal, volumetric and morphology data, J. Appl. Crystallogr. **44**, 1272 (2011).

[58] G. Kresse and J. Hafner, *Ab initio* molecular dynamics for liquid metals, Phys. Rev. B **47**, 558 (1993).

[59] G. Kresse and D. Joubert, From ultrasoft pseudopotentials to the projector augmented-wave method, Phys. Rev. B **59**, 1758 (1999).

[60] J. P. Perdew, K. Burke, and M. Ernzerhof, Generalized Gradient Approximation Made Simple, Phys. Rev. Lett. **77**, 3865 (1996).

[61] M. Imada, A. Fujimori, and Y. Tokura, Metal-insulator transitions, Rev. Mod. Phys. **70**, 1039 (1998).